Unified Shape and External Load State Estimation for Continuum Robots

James M. Ferguson, *Student Member, IEEE*, D. Caleb Rucker, *Senior Member, IEEE*
and Robert J. Webster III, *Senior Member, IEEE*

***Abstract*—Continuum robots navigate narrow, winding passageways while safely and compliantly interacting with their environments. Sensing the robot's shape under these conditions is often done indirectly, using a few coarsely distributed (e.g. strain or position) sensors combined with the robot's mechanics-based model. More recently, given high-fidelity shape data, external interaction loads along the robot have been estimated by solving an inverse problem on the mechanics model of the robot. In this paper, we argue that since shape and force are fundamentally coupled, they should be estimated simultaneously in a statistically principled approach. We accomplish this by applying continuous-time batch estimation directly to the arclength domain. A general continuum robot model serves as a statistical prior which is fused with discrete, noisy measurements taken along the robot's backbone. The result is a continuous posterior containing both shape and load functions of arclength, as well as their uncertainties. We first test the approach with a Cosserat rod, i.e. the underlying modeling framework that is the basis for a variety of continuum robots. We verify our approach numerically using distributed loads with various sensor combinations. Next, we experimentally validate shape and external load errors for highly concentrated force distributions (point loads). Finally, we apply the approach to a tendon-actuated continuum robot demonstrating applicability to more complex actuated robots.**

***Index Terms*—Soft robots, continuum mechanics, state estimation, stochastic processes, Gaussian process regression, continuous-time batch estimation**

I. Introduction

Continuum robots are compliant manipulators that bend continuously based on actuation and/or environmental interaction. A slender profile coupled with tentacle-like motion capabilities make continuum robots well-suited for a variety of applications that are challenging for traditional rigid-link robots. Thus, models have emerged which can compute a continuum robot's shape given actuator values and external loads applied to the robot [1]–[6]. However, unmodeled effects (e.g. tendon friction), and unknown external loads applied to the robot (e.g. environmental contact) will cause a discrepancy between the predicted shape of a robot and its actual shape. Therefore, sensors have been integrated into the robot to help infer its shape and external loading conditions.

This material is based upon work supported by the National Institutes of Health under Grant R01-EB026901 and the National Science Foundation under Grant EFMA-1935278, Grant NRI-2133027, and Grant IIS 1652588. Any opinion, findings, and conclusions or recommendations expressed in this material are those of the authors and do not necessarily reflect the views of the National Institutes of Health or the National Science Foundation.

J. M. Ferguson and R. J. Webster III are with Vanderbilt University, Nashville, TN 37235, USA, and D. C. Rucker is with The University of Tennessee, Knoxville, TN 37996, USA. Correspondence e-mail: james.m.ferguson@vanderbilt.edu, robert.webster@vanderbilt.edu

An early approach to incorporating sensors was simply to fit a parametric curve to a set of position measurements, without reference to the robot's mechanics-based model [7], [8]. Since robot models can provide additional prior information for improved accuracy, several groups have implemented model-based shape sensing techniques [9], [10]. Shi et al. [11] provide an extensive survey of continuum robot shape sensing methods. Overall, electromagnetic-tracking, intraoperative imaging, and fiber optic sensors have been successful. Of these, optical Fiber Bragg Grating (FBG) sensors have recently received considerable attention [12], [13], ultimately enabling FBG-based closed-loop control for continuum robots [14]–[18].

Since external forces act to deform continuum robots, shape sensing is actually coupled to external load sensing. Furthermore, external force knowledge is inherently useful in its own right. Researchers began estimating forces by assuming that the load was concentrated at the robot's tip; the 3D force vector was inferred based on sensor data [19]–[22]. Perhaps the most straightforward method to estimate tip force is to attach a small load cell to the distal end of the robot. While researchers have explored this approach [23]–[28], load cell size still precludes their application in many cases.

Instead of sensing tip forces directly, robot actuator efforts can be used to infer tip force without any additional hardware (i.e. intrinsic force sensing). Xu et al. first investigated intrinsic tip force sensing [19] for a push-pull style continuum robot. The method was expanded in [20] to consider estimation of full 6D wrenches at the robot's tip. Such intrinsic force sensing is an ongoing area of research and has recently been applied to parallel continuum robots [21].

The compliance of continuum robots also facilitates a deflection-based type of force sensing [29], [30]. Because the robot's shape is a function of the applied forces, loads can be estimated based on shape data. A probabilistic approach was explored by Rucker et al. [22] where tip force was estimated based on tip pose observations. The mapping between deflection and force was shown to be ill-conditioned, highlighting the need of a principled statistical solution. Recently, shape-based tip force sensing has been applied extensively to catheter robots in minimally invasive surgery [31]–[33]. While mainly used for shape sensing, FBG arrays have also been used for tip force sensing [34], [35].

Toward generalizing these approaches, researchers have dropped the tip force assumption to estimate multiple discrete loads along continuum robot backbones [36]–[39]. For non-slender soft robots, 3D finite element elasticity models can be inverted to map deflections to forces globally [40], [41],

but slender continuum robots have an ill-conditioned mapping, mainly due to their high axial stiffness. Nevertheless, shape-based estimation of distributed loads along a Cosserat rod was presented in [42] and extended to tendon-driven continuum robots in [43]. In this optimization approach, the force distribution was parameterized (e.g. Fourier series) so that shape error could be minimized by varying the parameters. The Gaussian force parameterization was designed to mitigate the ill-conditioning that is inherent to the distributed force sensing problem.

Due to ill-conditioning, all previous distributed load estimation efforts have made two simplifying assumptions on the nature of the external loads, which we detail in Section IV-A. Our method does not theoretically require these assumptions, but we do apply them in our experiments. Further, the assumptions are broadly applicable in low friction environments. Perhaps most notably, surgical robots and catheters [44] often interact with lubricious anatomical structures which impart minimal friction. Furthermore, normal forces often dominate friction in general, such as during smooth metal contact (e.g. aerospace inspection/repair [45]) and potentially underwater [45], where environmental contact would be lubricated. Moreover, even when friction is significant, it still may be useful to estimate normal forces alone. This approximation could be useful for contact detection or human-robot interaction.

While much progress has been made, force estimation work to date essentially treats shape data as a ground truth and relies on a fundamentally low-dimensional force parameterization to smooth the force estimate and make it robust to shape noise. Since shape measurements inherently contain uncertainty, we propose that they should be treated as such and estimated simultaneously in a statistically principled framework, explicitly accounting for the uncertainty in both shape and force. This enables Bayesian statistical inference to accomplish the smoothing, while keeping the force estimation high-dimensional. This approach has precedent in early work [22] which simultaneously estimated force and position at the tip only. Here we extend that basic philosophy to estimate force and position *everywhere* along the robot. Note that while estimation of continuum robot state in arclength has been previously explored [46], [47], external forces were not included in the model.

Our approach repurposes a concept originally developed for the time domain. Continuous-time batch estimation has been successfully applied to mobile robotics for localization and mapping tasks [48]–[50]. A mobile robot's state evolves over time, which is a single parameter. Analogously, the state of a continuum robot evolves over arclength, which is also a single parameter. Therefore, continuous-time batch estimation can be directly applied to the arclength domain.

Lilge et al. [51] have recently exploited this connection by using Gaussian process regression to elegantly estimate the shape of passive Cosserat rods directly on the special Euclidean group $SE(3)$ with good results. However, robot actuation was not incorporated in the model, and estimation of external forces was left to future work. In contrast, we show how to estimate both force and shape simultaneously, and the approach is built for general continuum robot models with actuation inputs, in addition to elastic rod models.

In this paper, we apply state estimation concepts to a general continuum robot model. As robot shape and applied loads are fundamentally coupled, we jointly estimate these functions along the robot backbone. The method is statistically principled: stochastic processes are estimated from observed data based on uncertain robot/measurement models, and uncertainties of all estimates are given. First, we apply the method to the Cosserat rod, which is the basis for many continuum robot models. We test the approach in simulation to estimate truly distributed loads, analyzing estimation error with a variety of practical sensor combinations. Next, we validate shape and highly concentrated point force estimates with experiments. Finally, we apply the approach to a tendon-actuated robot with promising results. The specific contributions of our work are:

1) A method for simultaneous estimation of continuum robot shape and external loads using continuous batch estimation on a general robot model.
2) Numerical analysis of the estimates produced by this method with distributed loads under many simulated sensor combinations.
3) Experimental analysis of the method with highly concentrated force distributions (point loads), using both a Cosserat rod and a tendon-actuated robot.

II. Robot State and Measurement Models

A. Continuum Robot Model

The mechanics model of a continuum robot describes how the state of the robot $\boldsymbol{\eta}$ evolves with respect to a spatial variable s: the distance along the robot's backbone. This state $\boldsymbol{\eta}$ typically contains kinematic variables which are related to internal mechanical strains. In general, distributed force and moment functions $\boldsymbol{v}_f(s), \boldsymbol{v}_l(s) : \mathbb{R} \mapsto \mathbb{R}^3$ act along the robot's backbone to continuously deform the robot's state. Note that while our method operates on distributed loads, it is possible to estimate concentrated force distributions (point loads) with our method (see Section VI). In this case, the estimated distribution should ideally be concentrated at the load application locations, approximating impulse functions.

Using the common "white noise notation" (see Appendix A), the continuum robot is modeled by a set of nonlinear, stochastic ordinary differential equations in the arclength parameter s:

$$\begin{aligned} \dot{\boldsymbol{\eta}}(s) &= \boldsymbol{h}(\boldsymbol{\eta}(s), \boldsymbol{v}(s), \boldsymbol{w}_\eta(s), s) \\ \boldsymbol{w}_\eta(s) &\sim \mathcal{GP}(0, Q_\eta \delta(s - s')) \end{aligned} \tag{1}$$

where we have stacked the input loading functions into a single vector: $\boldsymbol{v}(s) = (\boldsymbol{v}_f(s), \boldsymbol{v}_l(s))$. The robotic actuation variables (e.g. rod rotations, tendon tensions) take the form of boundary conditions for the above equation (see Section III-B).

To account for model inaccuracies (e.g. manufacturing imperfections), we adopt a standard approach of injecting zero-mean, white Gaussian noise $\boldsymbol{w}_\eta(s)$ into the state equation (1). The notation $\boldsymbol{w}_\eta(s) \sim \mathcal{GP}(0, Q_\eta \delta(s - s'))$ means that $\boldsymbol{w}_\eta(s)$ is a Gaussian process with a mean of zero and covariance function $Q_\eta \delta(s - s')$. The delta function is zero when computing the covariance between distinct points in arclength ($s \neq s'$); therefore the noise $\boldsymbol{w}_\eta(s)$ is not correlated in arclength (i.e.

white noise). The power spectral density matrix Q_η specifies the magnitude of the noise in each direction. Broadly speaking, a larger Q_η implies that more noise is injected into the model.

We additionally note that (1) implicitly parameterizes the Lie group $SE(3)$ into a vector space. In simple models, it is possible to define probabilities and perform estimation directly on $SE(3)$ [51]–[54]. However, computing the prior over $SE(3)$ with a general continuum robot model is not straightforward.

B. Stacked Robot and Distributed Load States

Given a prior distribution on the external load function $\boldsymbol{v}(s)$ and information about the boundary conditions (e.g. actuation variables), one could in principle compute the probability distribution of the state $\boldsymbol{\eta}(s)$ using stochastic integration. A very common approach would be to model the unknown process $\boldsymbol{v}(s)$ as Brownian motion:

$$\dot{\boldsymbol{v}}(s) = \boldsymbol{w}_v(s); \quad \boldsymbol{w}_v(s) \sim \mathcal{GP}(0, Q_v \delta(s - s')). \tag{2}$$

Again, the matrix Q_v is tunable: during estimation, a larger Q_v will produce quickly changing, noisy force estimates, and a smaller value will produce smoother functions.

Again using white noise notation (Appendix A), Equations (1) and (2) can now be stacked together into a single stochastic ordinary differential equation:

$$\begin{gathered} \dot{\boldsymbol{x}}(s) = \begin{bmatrix} \dot{\boldsymbol{\eta}}(s) \\ \dot{\boldsymbol{v}}(s) \end{bmatrix} = \boldsymbol{f}(\boldsymbol{x}(s), \boldsymbol{w}(s), s); \\ \boldsymbol{w}(s) \sim \mathcal{GP}(0, Q\delta(s - s')). \end{gathered} \tag{3}$$

The new process noise $\boldsymbol{w}(s)$ now encompasses both modeling uncertainty $\boldsymbol{w}_\eta$ as well as the white noise process $\boldsymbol{w}_v$ which controls the evolution of $\boldsymbol{v}(s)$. The reason for stacking the states together $\boldsymbol{x}(s) = (\boldsymbol{\eta}(s), \boldsymbol{v}(s))$ will be explained in the next section.

C. Solving an Inverse Problem with State Estimation

Previous literature has established that distributed load estimation in continuum robotics is fundamentally an inverse problem [43]. Indeed, the unknown distributed load function $\boldsymbol{v}(s)$ is an input to the state equation (1), and this input is to be determined from some measured output. The current approach is to parameterize the distributed load functions (e.g. Fourier series) and then least-squares solve for the coefficients which match the model with the measurements as closely as possible. Our approach instead transforms the inverse problem into a state estimation problem.

The reason for the stacking in (3) is so that we can use powerful state estimation techniques to estimate the full state-curve $\boldsymbol{x}(s) = (\boldsymbol{\eta}(s), \boldsymbol{v}(s))$, which includes both shape and external load information. By defining a dynamic model for $\boldsymbol{v}(s)$ and then stacking it together with the robot states $\boldsymbol{\eta}(s)$, we no longer have an unknown input function, and all of the unknowns can be estimated. The overall approach of stacking unknown inputs into the state is a common and effective approach [49] but has not been previously applied to external load estimation.

It is important to note that state estimation also allows for the estimation of static system parameters. Such unknown parameters can be stacked into the state as well, and their derivatives should be set to zero in (3). We used this approach in our experiments (Section VI) to calibrate our rod's bending stiffness.

D. Nonlinear Measurement Model

Given the prior model, we seek to incorporate sensor data for accurate estimation. We assume a general nonlinear discrete measurement model of the form

$$\boldsymbol{y}_k = \boldsymbol{g}(\boldsymbol{x}(s_k), \boldsymbol{n}_k, s_k), \tag{4}$$

where $\boldsymbol{y}_k \in \mathbb{R}^m$ is a measurement at arclength s_k and $\boldsymbol{n}_k \sim \mathcal{N}(0, R_k)$ is zero-mean Gaussian measurement noise with covariance R_k.

This model could represent any system which produces data corrupted by noise from continuum robot states. In this paper, we specifically consider position measurements as well as surface strain measurements along the robot.

III. Continuous-Arclength Batch Estimation

Continuous batch estimation is a method to estimate a continuous state-curve $\boldsymbol{x}(s)$ given a dynamic model $\boldsymbol{f}$ and noisy observations $\boldsymbol{y}_k$ based on a measurement model $\boldsymbol{g}$. We emphasize that batch estimation does not recursively step along arclength. Instead, the entire function $\boldsymbol{x}(s)$ is solved for in one optimization given the full batch of measurements $\boldsymbol{y}_k$. This is an established approach in the time domain [50], [55], [56] and has been applied to a Cosserat rod model for shape estimation [51]. Here we explain continuous batch estimation for a general continuum robot model (3).

In particular, we use the Gaussian process regression approach [49] which has been used for simultaneous trajectory estimation and mapping for mobile robots [48]. In this section, we outline the approach for continuum robots and point the reader to [49] for a detailed explanation of the underlying algorithm.

A. Gaussian Process Regression

In this method, a continuous Gaussian process [57] is fit to both the dynamic model (3) and the measurements (4) simultaneously. Given boundary conditions (Section III-B), the model (3) represents a continuous prior distribution of the robot state. We assume that this prior can be written as a Gaussian Process

$$\boldsymbol{x}(s) \sim \mathcal{GP}(\check{\boldsymbol{x}}(s), \check{P}(s, s')), \qquad s, s' > s_0 \tag{5}$$

specified by the mean and covariance functions $\check{\boldsymbol{x}}(s)$ and $\check{P}(s, s'))$ in arclength. We note that there is substantial literature for generating such distributions using methods of error propagation on motion groups [58]–[60].

Among other quantities, the state vector $\boldsymbol{x}(s)$ contains both shape and external load information (see (3)). Therefore, given (5), we immediately have prior distributions for both the robot

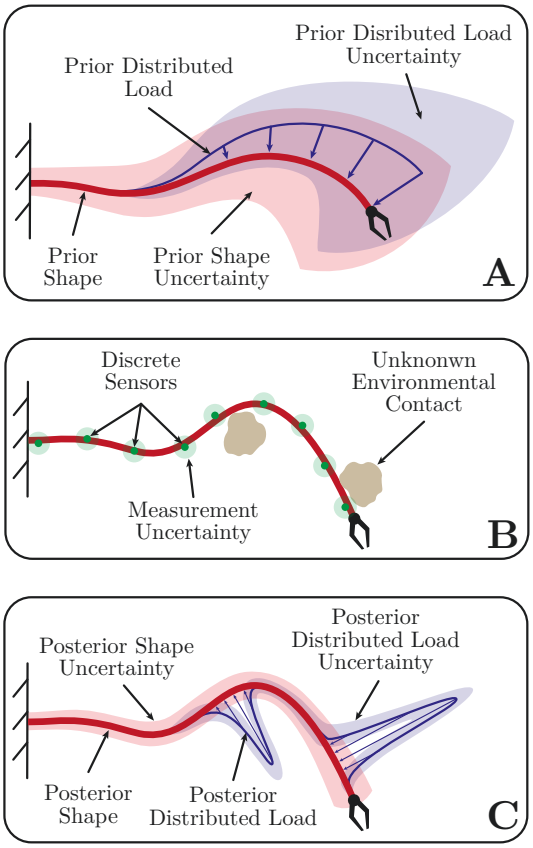

Fig. 1. Prior knowledge about robot shape (from mechanics models) and external loads is combined with observed data to produce a continuous posterior estimate of both shape and distributed loads simultaneously. Importantly, uncertainties (shaded regions) in the prior and measurements are mapped to uncertainties in the estimate.

shape and distributed load functions (see Figure 1A). In the figure, the two solid lines indicate the prior means based on $\check{\boldsymbol{x}}(s)$. The shaded regions represent the prior uncertainties, based on the covariance function $\check{P}(s, s'))$.

As mentioned, the estimator combines the prior (5) with measured data (Figure 1B) to produce the posterior distribution of the continuum robot state, which is also a Gaussian process:

$$\boldsymbol{x}(s) \sim \mathcal{GP}(\hat{\boldsymbol{x}}(s), \hat{P}(s, s')), \qquad s, s' > s_0. \tag{6}$$

The posterior mean and covariance functions $\hat{\boldsymbol{x}}(s)$ and $\hat{P}(s, s')$ together form the best estimate of the robot state given all available information. Accordingly, the robot shape and external load functions can be immediately extracted from (6), as illustrated by Figure 1C. Thus, estimation solves for the optimal mean functions (solid lines in 1C). The covariance functions (shaded regions in 1C) are also updated and are ideally much smaller than in Figure 1A indicating a precise solution.

The posterior (6) is essentially computed by solving an optimization problem with two cost terms: one for deviations from the prior (5) and one for deviations from the measurements (4). This is implemented by combining linearized-Gaussian estimation with the Gaussian process interpolation equations in one dimension [57]. The algorithm is iterative and updates both the prior and the posterior functions in each iteration to eventually produce the ultimate goal: $\hat{\boldsymbol{x}}(s)$ and $\hat{P}(s, s'))$. Because this algorithm translates directly from the time domain, we point the reader to Chapter 4.4 of [49] for details.

B. Imposing Boundary Conditions

State information at the endpoints is often necessary in continuum robot computations [1], [4]. For example, pose is often known at the robot base, and internal strain known at the tip. Notably, robotic actuation variables also manifest as boundary values (e.g. tendon actuation tensions) which must be incorporated. We impose such boundary values using a "soft constraint" approach described here.

In the algorithm, we are free to specify the prior distribution at the base of the robot $(\check{\boldsymbol{x}}(s_0), \check{P}(s_0))$ based on known boundary values. Note that these values can be found in [49] as the first entries in the "lifted prior":

$$\check{\boldsymbol{x}} = \begin{bmatrix} \check{\boldsymbol{x}}(s_0) \\ \vdots \\ \check{\boldsymbol{x}}(s_K) \end{bmatrix}, \quad \check{P} = \left[\check{P}(s_i, s_j)\right]_{ij}. \tag{7}$$

However, we usually only know partial state information at the base (e.g. pose but not strain). Therefore, we set the known variables in $\check{\boldsymbol{x}}(s_0)$ (e.g. pose) to their measured values and all other values to zero. Our confidence in the different components of $\check{\boldsymbol{x}}(s_0)$ is reflected in $\check{P}(s_0)$ appropriately. For the known quantities (e.g. pose), the covariance is set to small values. For the unknown quantities (e.g. strain), the covariance is set to a large number so that there will be minimal cost associated with large deviations. The tip boundary value works similarly but with the prior distribution $(\check{\boldsymbol{x}}(s_K), \check{P}(s_K))$.

We note that while boundary information is common, these soft constraints can actually be set at any point in arclength. This could be exploited to define a remote center of motion for example [47]. Furthermore, soft constraints naturally enable the incorporation of boundary value uncertainties, which could be useful with noisy actuators.

These soft boundary values also enable a straightforward method for 3D tip force sensing. If tip loads are expected, one could set the prior internal strain covariance to a reasonably high value at the tip. After estimation, posterior strain can be directly converted into sensed tip loads (and uncertainties).

IV. Cosserat Rod Model Application

As a first step toward more complex continuum robots, here we apply the method to the Cosserat rod model that we use in our experiments (see Figure 2). The shape is described by the position of the rod center line $\boldsymbol{p}(s)$ and its rotation matrix $R(s) \in \mathrm{SO}(3)$ which vary with arclength s. These functions are related to the linear and angular rates $\boldsymbol{q}(s)$ and $\boldsymbol{u}(s)$ by

$$\begin{aligned} \dot{\boldsymbol{p}} &= R\boldsymbol{q} \\ \dot{R} &= R\hat{\boldsymbol{u}}, \end{aligned} \tag{8}$$

where the $\hat{\cdot}$ operator generates skew-symmetric matrix from the space $\mathbb{R}^3$ as defined in [61].

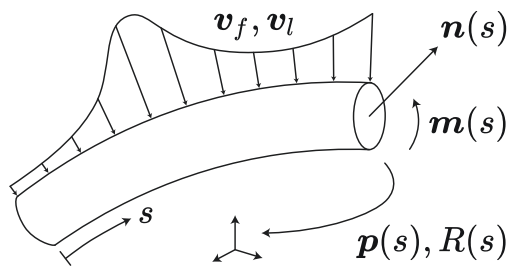

Fig. 2. Illustration of the geometric quantities in the Cosserat rod model.

For state estimation, it is generally more convenient to use a minimal representation for R [50]. We choose to represent R using XYZ Euler angles $\boldsymbol{\theta} \in \mathbb{R}^3$. We can write out R as

$$R = \begin{bmatrix} c_2c_3 & -c_2s_3 & s_2 \\ s_1s_2c_3 + c_1s_3 & -s_1s_2s_3 + c_1c_3 & -s_1c_2 \\ -c_1s_2c_3 + s_1s_3 & c_1s_2s_3 + s_1c_3 & c_1c_2 \end{bmatrix} \tag{9}$$

where, for example, c_2 stands for $\cos\theta_2$. We can differentiate this matrix and substitute into $\dot{R} = R\hat{\boldsymbol{u}}$ to obtain the following useful relationship between curvature and Euler angle rates [62]:

$$\dot{\boldsymbol{\theta}} = \begin{bmatrix} \frac{c_3}{c_2} & -\frac{s_3}{c_2} & 0 \\ s_3 & c_3 & 0 \\ -\frac{s_2c_3}{c_2} & \frac{s_2s_3}{c_2} & 1 \end{bmatrix} \boldsymbol{u} = S^{-1}\boldsymbol{u}. \tag{10}$$

We note that this representation does introduce a singularity (i.e. when $\cos\theta_2 = 0, S$ loses rank), but we did not observe ill-conditioning in our experiments because we designed the apparatus to avoid such configurations.

Thus, written in terms of material strains, the full Cosserat rod model is

$$\begin{aligned} \dot{\boldsymbol{p}} &= R\boldsymbol{q} \\ \dot{\boldsymbol{\theta}} &= S^{-1}\boldsymbol{u} \\ \dot{\boldsymbol{q}} &= \dot{\boldsymbol{q}}^* - K_{\text{se}}^{-1}((\hat{\boldsymbol{u}}K_{\text{se}} + \dot{K}_{\text{se}})(\boldsymbol{q} - \boldsymbol{q}^*) + R^T\boldsymbol{v}_f) \\ \dot{\boldsymbol{u}} &= \dot{\boldsymbol{u}}^* - K_{\text{bt}}^{-1}((\hat{\boldsymbol{u}}K_{\text{bt}} + \dot{K}_{\text{bt}})(\boldsymbol{u} - \boldsymbol{u}^*) \\ &\qquad + \hat{\boldsymbol{q}}K_{\text{se}}(\boldsymbol{q} - \boldsymbol{q}^*) + R^T\boldsymbol{v}_l) \\ \dot{\boldsymbol{v}}_f &= \boldsymbol{w}_f \\ \dot{\boldsymbol{v}}_l &= \boldsymbol{w}_l, \end{aligned} \tag{11}$$

where $\boldsymbol{v}_f(s)$ and $\boldsymbol{v}_l(s)$ are the distributed force and moment as shown in Figure 2, and $\boldsymbol{w}_f$ and $\boldsymbol{w}_l$ are their related white noise processes. These loading states cause changes in the linear and angular rates $(\boldsymbol{q} - \boldsymbol{q}^*)$ and $(\boldsymbol{u} - \boldsymbol{u}^*)$ relative to their original values $\boldsymbol{q}^*$ and $\boldsymbol{u}^*$. These changes are fundamentally caused by local shear/elongation K_{se} and bending/torsion K_{bt} effects.

A very common scenario is that the rod is initially straight with negligible shear and extension effects compared to bending/torsion [1]. In this case, the equations reduce considerably:

$$\begin{aligned} \dot{\boldsymbol{p}} &= R\boldsymbol{e}_3 \\ \dot{\boldsymbol{\theta}} &= S^{-1}K_{BT}^{-1}R^T\boldsymbol{m} \\ \dot{\boldsymbol{n}} &= -\boldsymbol{v}_f \\ \dot{\boldsymbol{m}} &= -\dot{\boldsymbol{p}} \times \boldsymbol{n} - \boldsymbol{v}_l \\ \dot{\boldsymbol{v}}_f &= \boldsymbol{w}_f \\ \dot{\boldsymbol{v}}_l &= \boldsymbol{w}_l, \end{aligned} \tag{12}$$

where $\boldsymbol{e}_3 = (0, 0, 1)$ and the internal moment $\boldsymbol{m}$ is related to the curvature $\boldsymbol{u}$ by

$$\boldsymbol{m} = RK_{\text{bt}}(\boldsymbol{u} - \boldsymbol{u}^*). \tag{13}$$

In our rod experiments (Section VI), the measured base pose and the assumed zero tip strain were used as boundary conditions.

A. External Load Assumptions for Experiments

Our overall method (Sections II and III) is general and imposes no constraints on the distributed loading functions $\boldsymbol{v}_f$ and $\boldsymbol{v}_l$. However, in our experiments, we make two simplifying assumptions on the nature of these functions. As discussed in Section I, ill-conditioning has made these assumptions standard for distributed loads, but they are broadly applicable when normal forces dominate friction.

First, a standard assumption in force sensing literature is that the distributed moment function $\boldsymbol{v}_l(s)$ is zero [38], [42], [43]. Such distributed moments could possibly be caused by frictional surface contacts that impart a moment about the local robot backbone point. Therefore, neglecting distributed moments is a reasonable assumption when friction is negligible or when the robot is sufficiently thin, as is the case in our experiments. Note that $\boldsymbol{v}_l(s) = 0$ does not imply the absence of internal moments $\boldsymbol{m}$. External forces $\boldsymbol{v}_f(s)$ are still propagated through the state equation to produce nonzero $\boldsymbol{m}$.

Second, as noted by Khan et al., [35], slender robots generally have high axial stiffness relative to their bending stiffness such that axial strains are negligible. Thus, axial components of distributed force cannot reliably be estimated from strain or deflection data alone. Therefore, prior works [38], [42], [43] assume that the distributed force function $\boldsymbol{v}_f(s)$ is orthogonal to the rod backbone curve, and we also adopt this assumption for our experiments. This assumption is valid when neglecting friction forces which may occur in the axial direction [43]. Note that if tip force sensing is included in the estimation (see Section III-B), the tip force vector could still be a general 3D vector.

Now, the second assumption means that $\boldsymbol{v}_f$ must lie in the local $X - Y$ plane. Therefore, we can reparameterize $\boldsymbol{v}_f$ in the local frame in 2D: $\boldsymbol{v}_{xy}(s) : \mathbb{R} \mapsto \mathbb{R}^2$. After incorporating the two assumptions, the prior rod model becomes

$$\begin{aligned} \dot{\boldsymbol{p}} &= R\boldsymbol{e}_3 \\ \dot{\boldsymbol{\theta}} &= S^{-1}K_{BT}^{-1}R^T\boldsymbol{m} \\ \dot{\boldsymbol{n}} &= -R\begin{bmatrix} \boldsymbol{v}_{xy} \\ 0 \end{bmatrix} \\ \dot{\boldsymbol{m}} &= -\dot{\boldsymbol{p}} \times \boldsymbol{n} \\ \dot{\boldsymbol{v}}_{xy} &= \boldsymbol{w}_{xy} \end{aligned} \tag{14}$$

where

$$\boldsymbol{w}_{xy} \sim \mathcal{GP}(0, Q_{xy}\delta(s - s')).$$

Practically speaking, we can assume that the forces have equal variance in the local x and y directions so that $Q_{xy} = \text{diag}(Q_f, Q_f)$.

B. Measurements

We consider two main types of measurements in this paper. The first is the 3D position of the rod at known locations along the rod's backbone. This suggests the following observation equation:

$$\boldsymbol{g}_1(\boldsymbol{x}) = \boldsymbol{p} + \boldsymbol{n}_{k_1}, \tag{15}$$

where $\boldsymbol{n}_{k_1}$ is 3D Gaussian noise added to the position measurements.

In our simulations (Section V), we will additionally consider taking strain measurements along the rod. The general relationship between mechanical strains γ_{xy}, γ_{zy}, and ϵ_z and the kinematic quantities $\boldsymbol{u}$ and $\boldsymbol{q}$ is [63]

$$\begin{bmatrix}\gamma_{zx} & \gamma_{zy} & \epsilon_z\end{bmatrix}^T = (\boldsymbol{q} - \boldsymbol{q}^*) - \boldsymbol{r} \times (\boldsymbol{u} - \boldsymbol{u}^*), \tag{16}$$

where $\boldsymbol{r} = (x, y, 0)$ is the vector from the rod's neutral axis to the test point, expressed in the body frame. The strains γ_{zx} and γ_{zy} are the shear strains normal to the local z axis and in the local x and y directions respectively, while ϵ_z is the normal strain in the local z direction.

The practical scenario that we study in this paper is the case where at each arclength measurement point, we attach two strain gauges to the rod surface. This situation is motivated by FBG sensor arrays which can be used to infer 3D rod shape from elongation ϵ_z measurements.

In our simulations, we fix strain gauges at surface points $\boldsymbol{r} = (\rho, 0, 0)$ and $\boldsymbol{r} = (0, \rho, 0)$ to measure the normal strain ϵ_z. In other words, at each measurement point, two gauges are positioned 90° radially from one another, along the local X and Y axes. Plugging these in to (16) and stacking the two resulting ϵ_z's, we get the following observation equation:

$$\boldsymbol{g}_2(\boldsymbol{x}) = (v_3 - v_3^*) \begin{bmatrix}1\\1\end{bmatrix} + \rho \begin{bmatrix}-u_2\\u_1\end{bmatrix} + \boldsymbol{n}_{k_2}, \tag{17}$$

where $\boldsymbol{n}_{k_2}$ is 2D additive Gaussian noise. In the case that there is negligible shear or elongation, this simply reduces to

$$\boldsymbol{g}_2(\boldsymbol{x}) = \rho \begin{bmatrix}-u_2\\u_1\end{bmatrix} + \boldsymbol{n}_{k_2}. \tag{18}$$

Thus, two strain gauges used in this 90° radial configuration essentially serve to measure rod curvature, scaled by rod radius.

V. Distributed Load Simulations

Here we test the estimation approach in a wide variety of practical scenarios with a series of numerical experiments. Specifically, we apply truly distributed loads to the model to compare with estimation results. During each scenario, we analyze the effect on estimation accuracy of two noise variables: the number of measurements N and the measurement uncertainty σ. Ultimately, for each scenario, we build a heat map to analyze the relationship between estimation error and these two noise variables.

In our simulations, we compare two common data sources: position data $\boldsymbol{g}_1$ and strain measurements $\boldsymbol{g}_2$ taken along the rod. Furthermore, we consider two additional scenarios First, in order to improve distributed load estimation, we consider the case where the base load is measured by means of a 6 DOF force sensor. This is implemented by setting the prior boundary values for $\boldsymbol{n}(s_0)$ and $\boldsymbol{m}(s_0)$ to be their measured values (see Section III-B). Second, when using strain measurements, integration drift may become substantial at the tip; therefore, we consider the case where the tip position is additionally measured by means of an attached sensor (e.g. magnetic tracking coil). This is implemented by setting the final boundary value for $\boldsymbol{p}(s_f)$ to be the measurement.

In summary, we test four scenarios in our numerical experiments: i) position only, ii) position + base load, iii) strain only, and iv) strain + tip position. We vary the number of measurements N and the measurement uncertainty σ in each case.

A. Data Generation

To generate ground truth data, we chose to apply a linear combination of three Gaussian functions to the rod model. The idea is that distributed loads from environmental contact may resemble bell curves [43]. We note that the estimator does not know how this ground truth load profile was generated and assumes that the function has the general Brownian motion prior in (14). Each Gaussian function has four parameters: location along the rod, width of the curve, height, and the angle around the rod. Each parameter was chosen uniformly at random in simulation; the distributed load was formed by adding the functions together.

After generating ground truth applied loads, the Cosserat rod equations were solved using a standard shooting method to generate ground truth data sets. In our simulations, we use a 1.5 mm diameter solid rod with Young's modulus of 207 GPa. This process was repeated to produce 50 ground truth data sets.

B. Estimation Procedure

For each of the ground truth data sets, we test each of the four scenarios while varying both the two noise variables σ and N. For the position scenarios, we consider four levels of standard deviations σ: $10^1, 10^0, 10^{-1}$, and 10^{-2} mm. For the strain scenarios, we consider standard deviations σ of $10^2, 10^1, 10^0$, and 10^{-1} μ-strain. In all scenarios, we considered five different values for N: $5, 15, 50, 150$, and 500. Overall, this amounted to 80 different estimations for each of the 50 ground truth data sets. For each estimation, first the data set (either ground truth strain or position) was subsampled according to N and Gaussian noise was added to the measurements according to σ. Estimation was then performed with $Q_{xy} = \text{diag}(10^{-11}, 10^{-11})$. We note that during estimation, a small percentage of cases did not converge which could be remedied by a better initialization.

We detail the output from one example estimation scenario in Figure 3. In this example, the full state is estimated based on $N = 50$ strain measurements $\boldsymbol{g}_2$ which are corrupted by $\sigma = 10^0$ μ-strain of noise. Note that this is a strain + tip position example, which includes an embedded tip position sensor to mitigate strain integration drift.

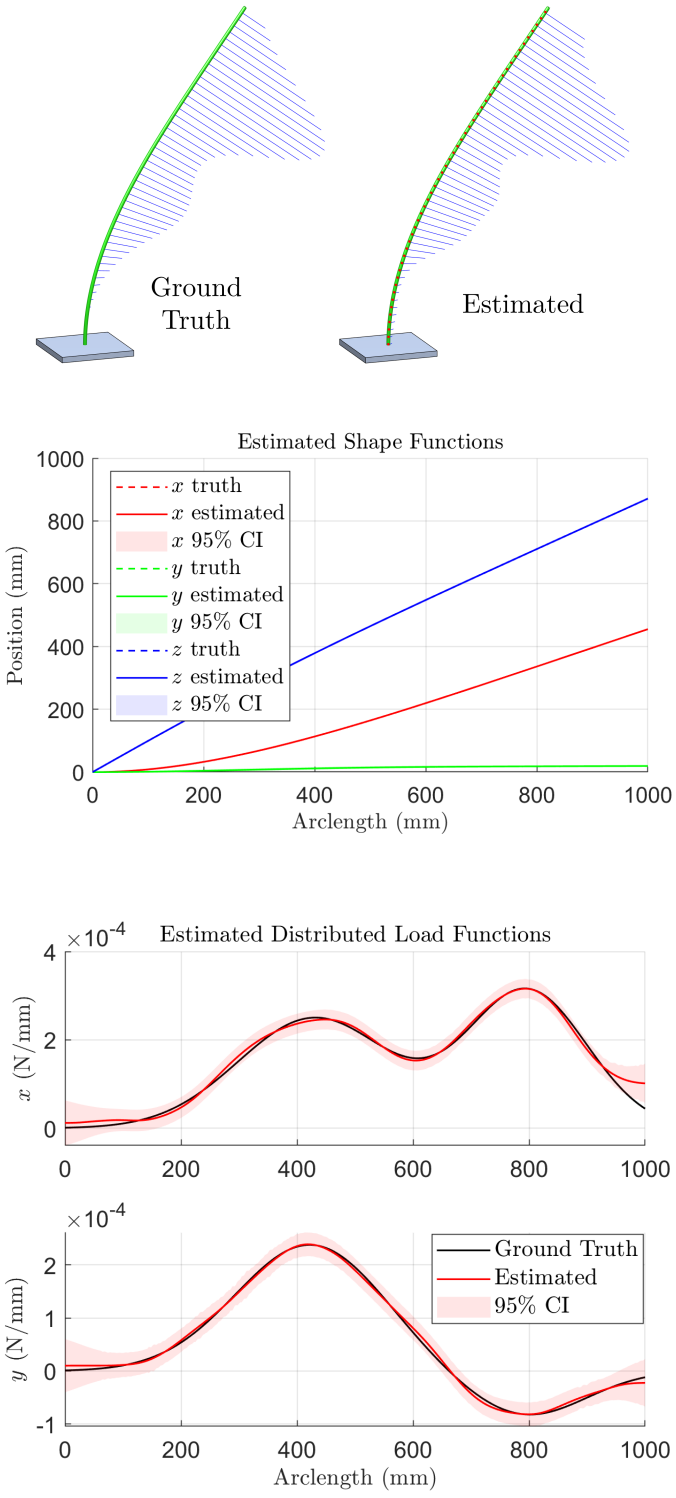

Fig. 3. Typical results taken from one of our 4000 shape/load estimation simulations. *Top:* In this example, estimation of the shape (green) and distributed loads (blue) is based on 50 bending strain sensors placed along to rod (red dots) and one single position sensor at the distal tip. *Center:* The shape estimation results indicate excellent agreement with the ground truth. Note that the small uncertainty cannot be visualized at this scale. *Bottom:* The external load estimation results show good agreement with the ground truth in this example.

All of such 4000 estimated states were then compared to their corresponding ground truth. Specifically, both the RMS shape and distributed load errors were computed with respect to arclength for each of these simulations. The errors were then averaged over all simulation cases for each combination of noise variables σ and N. Thus, average shape error $\boldsymbol{e}_p$ was plotted versus the two noise variables in a heat map in Figure 4. A similar heat map was constructed for distributed load error $\boldsymbol{e}_f$ in Figure 5. In both figures, plots of the four different sensing scenarios are shown for comparison. Note that we have normalized shape error $\boldsymbol{e}_p$ as a percentage of the rod's length and force error $\boldsymbol{e}_f$ as a percentage of the RMS applied load over all test cases.

In summary, in this section, we simulated many shape/load estimations using four different sensing scenarios and many different combinations of measurement noise variables for comparison. We used these simulations to generate heat maps (Figures 4 and 5) to illustrate the effect of the noise variables on shape and distributed load estimation error for each of the four sensing scenarios.

VI. Point Load Experiments

Here we experimentally evaluate our approach by applying point loads to deform a Cosserat rod; state estimation is based on position measurements taken from a laser scanner. To assess performance, we compare the estimate to measured values for both shape and external loads. Thus, shape error, force magnitude error, and force location error are all fully characterized.

In these experiments, we apply point forces, which are mathematically described by impulse functions. Ideally, the estimated force distribution should be concentrated at the ground-truth location. Due to the ill-conditioning present [43], this assessment actually represents a worst-case stress test for our method, which we later discuss (Section VIII-D). We note that while true distributed loads are possible to apply, they are not feasible to measure accurately for ground-truth comparison with the solution. Therefore, we follow prior work [42], [43] and evaluate truly distributed loads in simulation (Section V) and use point loads for our experiments.

A. Data Collection

To collect measured shape and force data, we used the setup shown in Figure 6. The FARO Quantum Max laser scanning arm (FARO Technologies, Inc., Lake Mary, FL, USE) is a mechanical linkage with several encoded joints with a laser scanner attached to its proximal link. Data from the encoders and the laser together enable 3D rod shape outputs. An ATI Mini 40 6D force/torque sensor (ATI Industrial Automation, Apex, NC, USA) was attached to the 500 mm Nitinol tube (radius 2 mm, wall thickness 0.2 mm) to measure applied forces.

During each test, weights were hung by cables passing through pulleys held in space by lockable holding arms. The

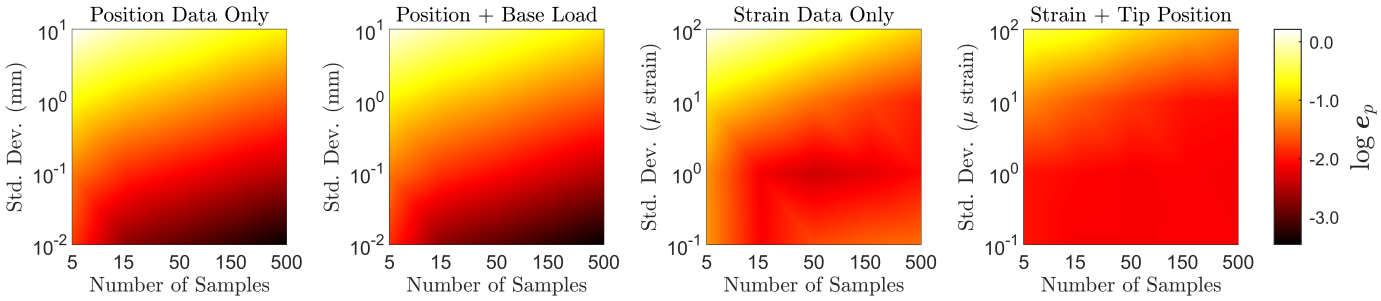

Fig. 4. Heatmaps showing average shape estimation error in our simulations. Note that shape error $\boldsymbol{e}_p$ is computed as a percentage of rod length which was 1 m. Our simulations considered four sensing scenarios: i) state estimation from position data only, ii) position data and a 6D force sensor at the base, iii) strain data only, and iv) strain data and a tip position sensor. In each case, estimation error varies based on the uncertainty and quantity of the measurements.

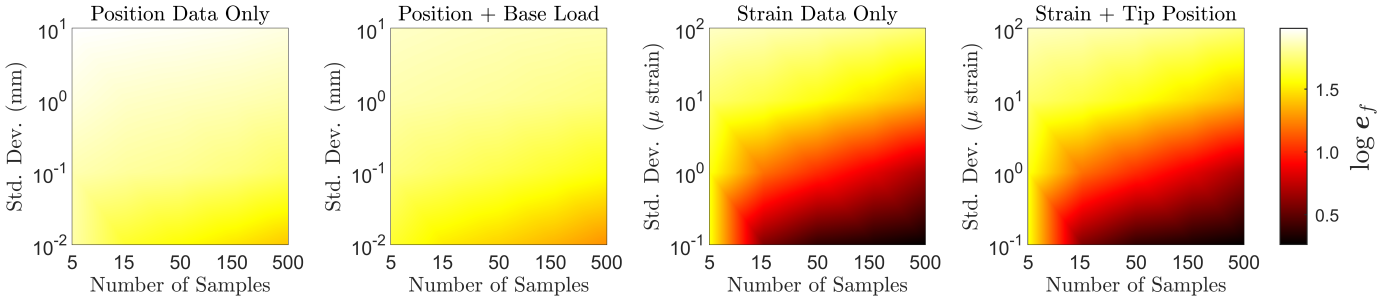

Fig. 5. Heat maps showing average distributed force estimation error in our simulations. Note that distributed force error $\boldsymbol{e}_f$ is computed as a percentage of the RMS applied force over all simulations which was 0.27 N/m.

weights used in each of our tests are recorded in Table I. The cables were then tied to the rod to force it into deflected shapes. A machinist square was used to ensure that the applied loads were normal to the rod.

The whole apparatus was then scanned with the laser scanning arm to capture the shape of the rod as well as the force application points. Special care was taken to sweep the laser scanner over the rod from base to tip multiple times to capture the pose of the rod accurately. A clustering algorithm based on fitting the rod surface data to consecutive cylinders was used to transform the acquired point cloud data into measurements $\boldsymbol{y}_k$ versus arclength s_k. Over our 9 data sets, the average number of backbone points was 258 after this process.

B. Estimating Rod Stiffness Parameter

The estimates output by our method depend on the rod's bending stiffness; therefore, it is crucial that this value be calibrated to achieve accurate force estimation. We note that anecdotally, our experiments depend minimally on the torsional stiffness, so we forgo torsional stiffness calibration in our experiments.

As noted in Section II-C, continuous-arclength estimation can also be used to estimate static parameters. This is how we calibrate the bending stiffness parameter k_b required for our experiments. Toward this, we first collected a data set (see Table I) of a known load applied to the rod's tip. As described in Section II-C, the unknown k_b is stacked the state, and we define the following state equation to model the rod under tip loading conditions:

$$\begin{aligned} \dot{\boldsymbol{p}} &= R\boldsymbol{e}_3 \\ \dot{\boldsymbol{\theta}} &= S^{-1}K_{BT}^{-1}R^T\boldsymbol{m} \\ \dot{\boldsymbol{m}} &= -\dot{\boldsymbol{p}} \times \boldsymbol{n} \\ \dot{k}_b &= 0 \end{aligned} \tag{19}$$

where we note that $\boldsymbol{n}$ is constant and equal to the applied load, and $\boldsymbol{v}_f = 0$ because only tip loading was present. Because the rod was uniform in arclength, the bending stiffness parameter is constant ($\dot{k}_b = 0$). We note that even though the parameter is static, its constant mean and variance functions are unknown until the calibration is complete.

Given the measured position data, this system is then estimated using the same algorithm as before to determine the state versus arclength (including the constant bending stiffness). The results of this process, including the theoretical values of k_b based on rod geometry with a Young's modulus of 50 GPa, are shown in Table II.

C. Dependence on Q_f

The results of our shape/load estimation depend heavily on the power spectral density matrix $Q_{xy} = \text{diag}(Q_f, Q_f)$. A large value for Q_f would allow for a more noisy, quickly changing force distribution, but a small Q_f would yield slowly changing, smooth force estimates. This is illustrated in Figure 7 where we have performed our estimation (using the One Force 1 data set) with different values for Q_f. As shown in the figure, a value of $Q_f = 10^{-9}$ strikes a compromise between

TABLE I
TABLE OF APPLIED LOAD MAGNITUDES AND CORRESPONDING ARCLENGTH POSITIONS FOR ROD ESTIMATION EXPERIMENTS

	Calibration	One Force #1	One Force #2	One Force #3	One Force #4	One Force #5	Two Force #1	Two Force #2	Two Force #3
Load 1 Magnitude (N)	0.49	0.15	0.25	0.59	0.35	0.27	0.69	0.98	0.98
Load 1 Arclength (mm)	177	275	275	141	234	215	163	180	162
Load 2 Magnitude (N)	—	—	—	—	—	—	0.30	0.35	0.35
Load 2 Arclength (mm)	—	—	—	—	—	—	372	416	406

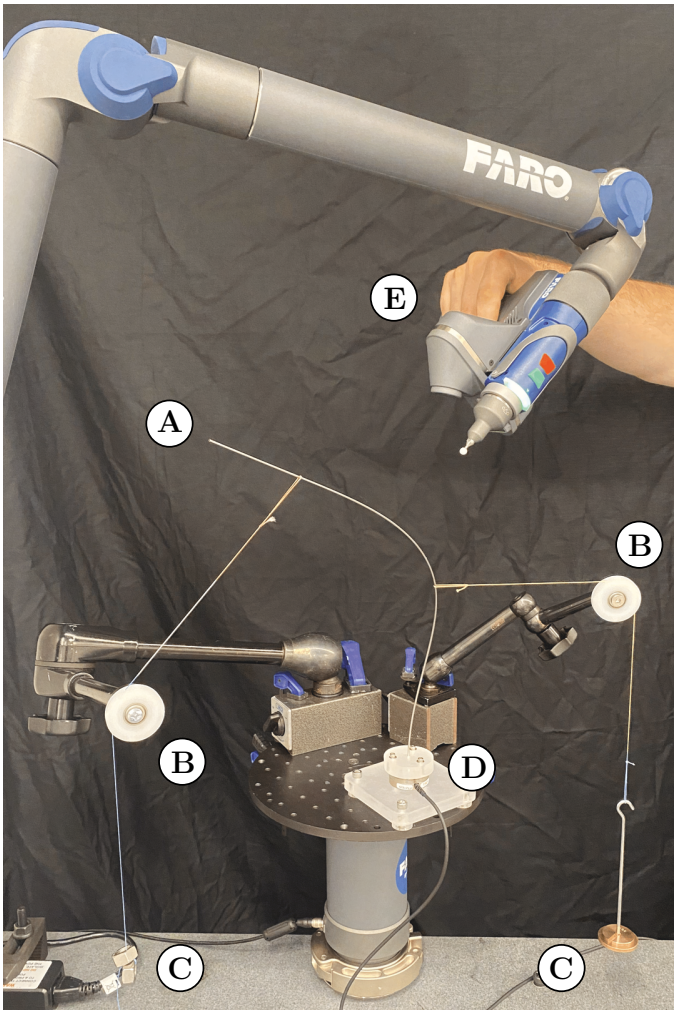

Fig. 6. Experimental setup to measure both the shape and point loads along a rod (A). Weights (C) are hung by cables through pulleys (B) attached to the test jig to apply point loads deforming the rod. During loading, thousands of rod shape measurements are collected by a laser scanning arm (E). This scanner additionally provides the location of the point forces. A force sensor attached to the rod base (D) provides the forces themselves. Knowledge of shape and applied loads enables evaluation of our method.

TABLE II
CALIBRATION OF THE BENDING STIFFNESS PARAMETER k_b (KN-MM^2) FOR THE NITINOL ROD USED IN OUR EXPERIMENTS.

	Prior	Calibrated
Value	23.05	8.33
Std. Dev.	100.0	0.32

load centralization and noise rejection, which we discuss in Section VIII-D. Therefore, we qualitatively choose to use this value throughout our experiments.

D. State Estimation Accuracy

To achieve the best case results, we first ran our estimator on each of our 8 data sets using all of the available shape measurements. The resulting estimated rod shapes and force distributions as well as the measured point loads are shown in Figure 8.

Next, we quantitatively evaluate the ability of our method to estimate force magnitude and location along the rod. To do this, we perform a series of estimations with the five One Force data sets. For each data set, we perform an estimation down sampling to 3, 5, 10, 25, 50, 100, and 200 position measurements. For each estimation, we first compute the RMS position error between the estimated shape and the measured shape. Next, we integrate the estimated distributed load across the rod. This value should be equal to the force acquired from the load sensor at the rod base, so we take the norm of this difference to be the force magnitude error. Finally, we take the location of the maximal value of distributed load as our estimate of the force location. Therefore, the difference between this value and the force location based on the laser scanner was taken as the force location error. These errors in each data set were then averaged across the different numbers of measurements. The results are shown in Figure 9.

Finally, we qualitatively evaluate the effect of the number of shape measurements on the estimated distributed load. Toward this, we subsampled the One Force 1 data set to 5, 50, and 200 data points and performed estimation in each case. The results are shown in Figure 10.

VII. ESTIMATION WITH A TENDON-ACTUATED ROBOT

To demonstrate the method on a more complex continuum robot, we next applied the method to the tendon-actuated robot in Figure 11, which has been used in prior work on external force sensing [43]. The robot's 1.4 mm diameter circular backbone was made of a 40 cm length of spring steel. A single actuated tendon, 14 mm away from the backbone, was routed through 9 spacer disks spaced in 5 cm intervals. Optical markers were attached to each of the spacers for 3D tracking. A linear actuator was used to prescribe the length of the

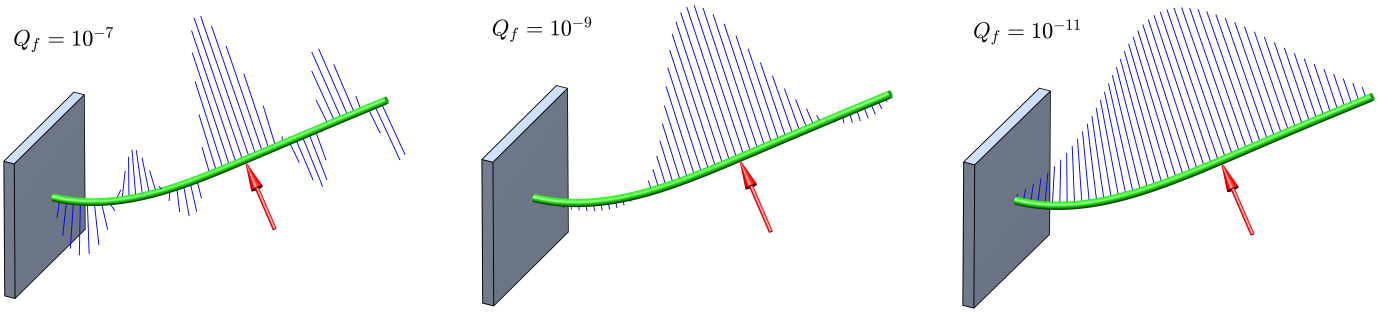

Fig. 7. Effect of Q_f on distributed load estimation. Larger values allow for quickly changing force profiles which can overfit to noise (left). Small values result in more smoothly varying estimates which may not capture the concentrated nature of point loads (right). We chose a compromise between load centralization and noise rejection (center).

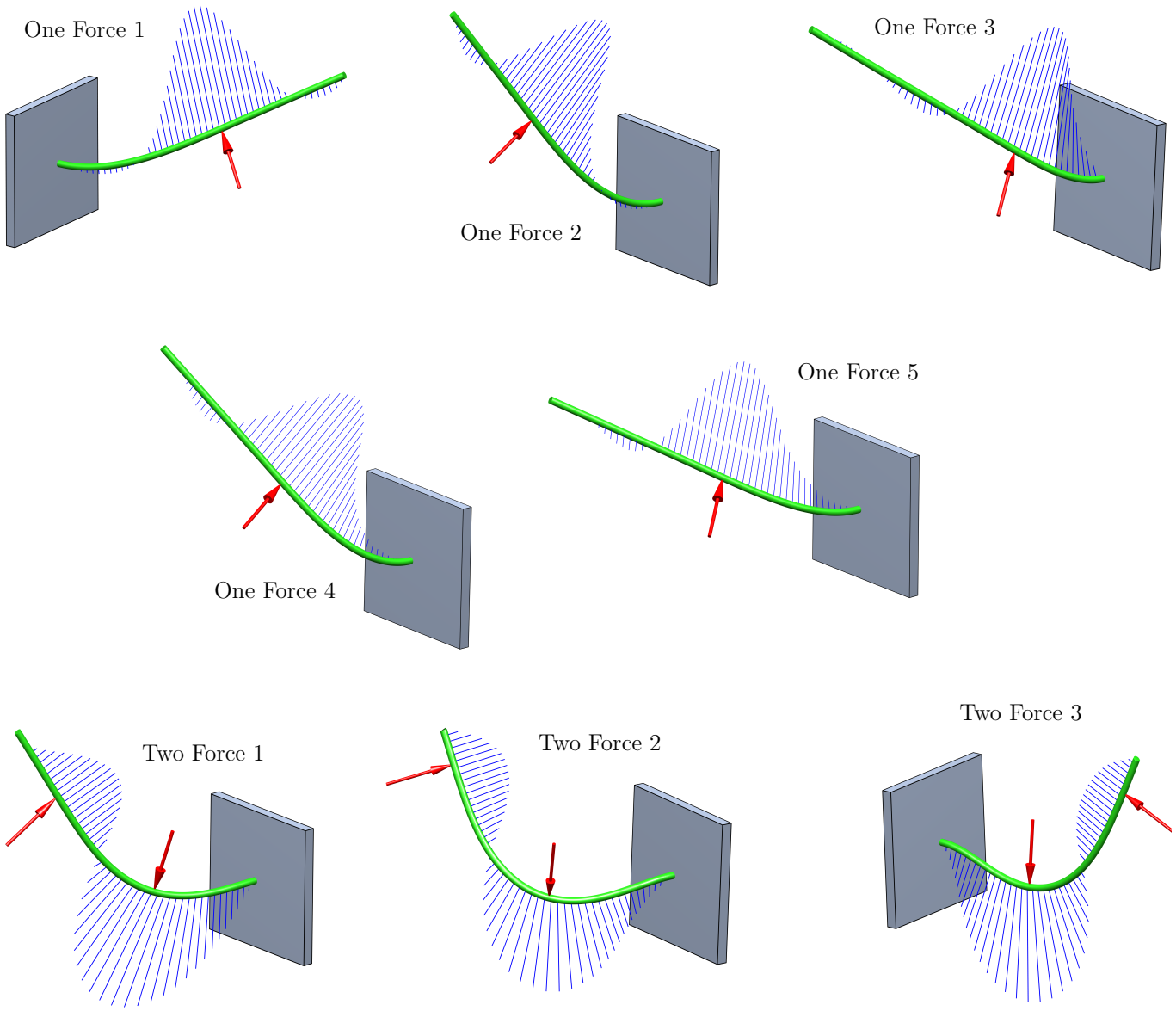

Fig. 8. Estimated shape and distributed load profiles for the 8 data sets. For each test case, the green tube illustrates the estimated rod shape, the red arrow represents the known (from laser scanner) point load on the rod, and the blue arrows represent the estimated distributed load along the rod.

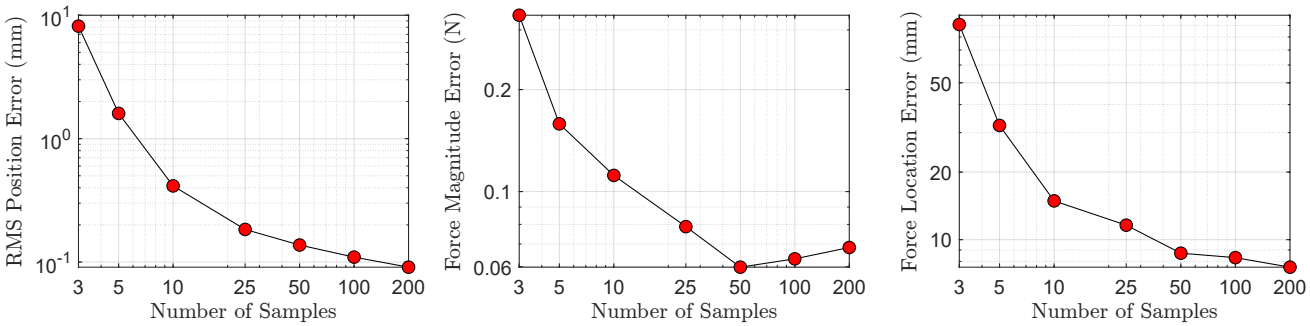

Fig. 9. Experimental estimation accuracy versus number of position measurements. RMS position error (Left), force magnitude error (Center), and force location error (Right) are shown. Errors are averaged over our 5 One Force data sets.

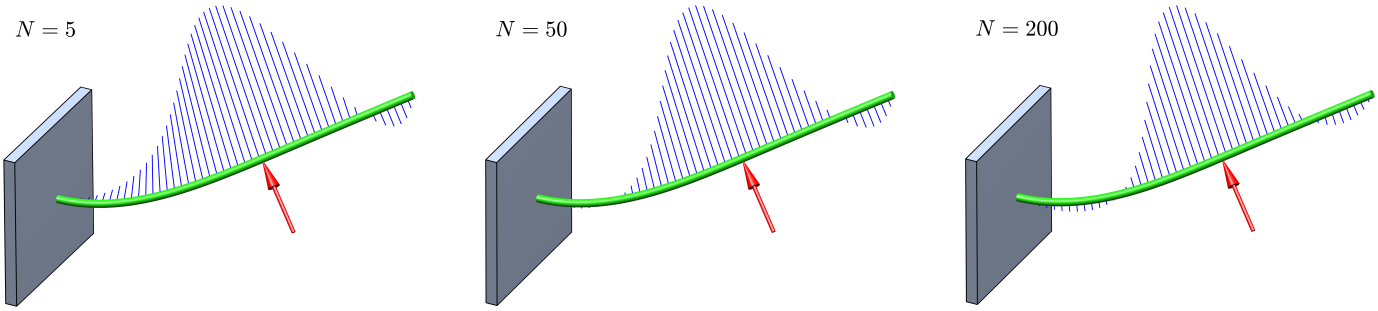

Fig. 10. Effect of the number of position measurements on estimated external load for the One Force 1 data set. More measurements result in distributed loads that are more centralized, and reasonably good results can be achieved with relatively few data points.

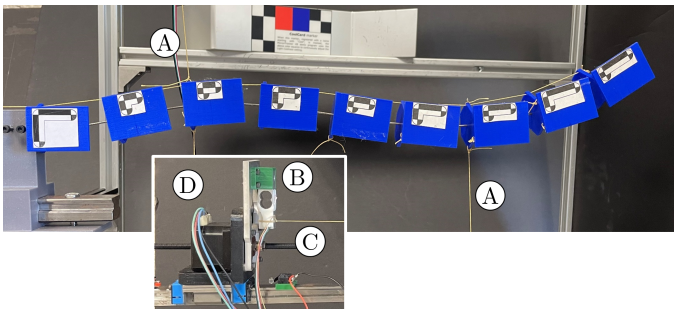

Fig. 11. Setup to apply our method to a tendon-actuated continuum robot. Strings (A) are attached to the robot for external load application. A single tendon (C) is tensioned by a linear actuator (D) to deform the robot. All strings terminate at load cells (B) for force measurement.

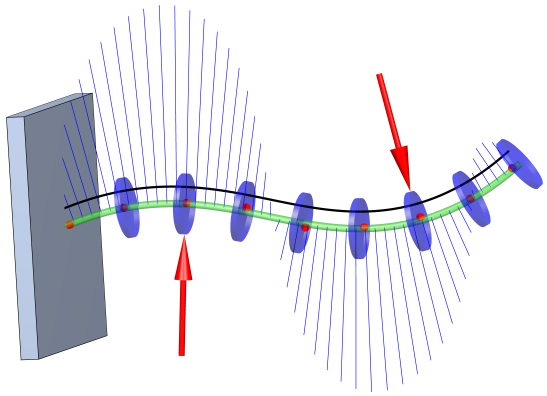

Fig. 12. Tendon robot estimation example. The backbone shape closely matches the acquired position data points (red dots), and the shape of the distributed load function roughly approximates the applied point loads (red arrows).

tendon with a load cell in line to measure tendon tension. For load application, Kevlar threads were attached at two points on the robot. The opposite ends were fixed to load cells for measurement.

The tendon was actuated to 2.0 cm, and two loads (6.44 and 1.24 N) were applied to the robot at $s = 10$ and $s = 30$ cm. The positions of the optical markers were measured with a Micron tracker, and (with known offsets) produced 9 measurements along the backbone. These position measurements were the data $\boldsymbol{y}_k$ used for estimation.

We used the general tendon routing model in [4] to model the robot. Again, this was stacked with $\dot{\boldsymbol{v}}_{xy}$ to form the full set of state equations. Given this model, $\boldsymbol{y}_k$, and appropriate tip boundary conditions (tendon tension and moment), the estimation was performed. The results are shown in Figure 12.

VIII. Discussion

A. Shape Estimation

Overall, accurate shape estimation did not require very many measurements. Indeed, we achieved errors of less than 2% of the rod's length with 5 measurements in simulation (Figure 4), and only 3 position measurements in our experiments (Figure 9). When estimating from strain measurements, addition of a tip position sensor significantly reduced the shape error when using few or noisy strain measurements in our simulations (Figure 4).

Overall, strain and position measurements yielded comparable shape errors in our simulations. Both data sources were able to quickly achieve submillimetric error as the number of measurements increased (or as noise decreased). Therefore, either position or strain data are appropriate for shape estimation. If the number of strain sensors is small or the sensors are noisy, a tip position sensor could further improve accuracy.

B. Distributed Load Estimation

In our simulations (Figure 5), the distributed force functions matched the ground truth curves better when using strain measurements, as opposed to position. With strain measurements, the average RMS distributed load error could be brought down to a reasonable 1.8% of the RMS applied distributed loads. In the specific case of a sensor with 1 μ strain of error, this average error was about 5% with 500 strain measurements (which could be reasonable when using an FBG array).

When instead using position measurements, the error was 26% in the best case (500 measurements with 0.01 mm of position noise). With an additional base force sensor, error could be further improved to 18%. Overall, strain measurements appear to be superior to position measurements for distributed load estimation. If only position data is available, performance could be improved by adding a base force sensor.

C. Point Load Estimation

In our point load experiments, the method performed well in terms of average force magnitude error (0.07 N) and force location error (7.5 mm) compared with [42] (0.3 N and 6 mm). Additionally, we found that only a few position data points need to be gathered for good force estimation results (Figure 10). However, diminishing returns were seen only after 50 position data points.

While our method can handle general applied loads, we chose to apply standard external load assumptions in our experiments (see Section IV-A). Future work could relax these assumptions in order to experimentally validate our method in high friction environments. Note that this may exacerbate ill-conditioning; more sensing/data could be required for accurate results.

Additionally, the ground-truth loads in our simulations were smooth distributed functions (see Figure 3); however, the wires in our experiments applied highly concentrated force distributions (point loads) to the robot. While smooth force distributions could be produced experimentally, it is very challenging to measure a ground-truth distributed load function. That is why we followed the point load conventions in the literature [42], [43] in our physical experiments (Section VI) and verified the ability to estimate smoothly varying distributed loads in simulation (Section V), where exact ground-truth is available. Verifying smooth distributed loads in physical experiments could be another topic for future work.

D. Ill-Conditioning and Choice of Prior

When estimating point loads, the force distribution should ideally be concentrated at the point of application, closely approximating an impulse function. There is a significant difference between the applied loads and our estimated distributions in Figure 8: the continuous estimation does not fully capture the concentrated nature of the point load in many of our results. Nevertheless, the reconstructed shape is accurate, which highlights the ill-conditioning present in the problem [43]. The "sharpness" of the estimated distributed load (and thus its ability to capture truly concentrated loads) is dictated by the prior parameter Q_f in our approach. More highly concentrated estimations are possible if Q_f is larger, but this comes with the trade-off of increased susceptibility to noise (see Figure 7), which is again due to the ill-conditioning. Thus, our concentrated loading experiment actually represents the most challenging case on which to test our estimation approach: a worst-case "stress test".

While this ill-conditioning could be improved by using strain measurements instead of position, it can also be partially explained by our choice of prior on the distributed load process $\boldsymbol{v}_f(s)$. While mathematically convenient, Brownian motion (2) may not capture typical distributed force profiles, especially concentrated ones. Therefore, better results could be achieved with a prior $\boldsymbol{v}_f(s)$ which more closely matches the types of functions expected. In prior work, this was accomplished by choosing appropriate parameterizations (e.g. combinations of Gaussians) for the distributed load $\boldsymbol{v}_f(s)$ and then least-squares solving for the coefficients [43]. This approach basically constrains the prior on $\boldsymbol{v}_f(s)$ directly, and future work could statistically formalize such a prior with a state estimation approach.

E. Tendon Robot Estimation and Efficiency

Our tendon-driven robot results (Figure 12) demonstrate that our method is feasible on actuated prototypes. Indeed, the estimated shape of the robot's backbone closely matched the acquired data with 4.1 mm RMS position error between the optically tracked points and the model. Furthermore, the shape of the distributed force function was a reasonable approximation to the applied point loads, given the low number of position measurements available.

Across our experiments, the average run time was 4.01 seconds. Currently, this is not fast enough for real-time application. This is at least partly because our prototype method was implemented in MATLAB with minimal code optimization. With careful implementation in a compiled language running on powerful hardware, the method could be made many times faster, approaching real-time application.

IX. CONCLUSION

In this paper, we proposed a method which simultaneously estimates continuum robot shape and external loads. We first performed a series of simulations to analyze the method's performance with distributed applied loads in a variety of scenarios. Second, we experimentally evaluated our method in the practical case of point load application achieving shape errors of 2% of the rod's length with only 3 position measurements taken along the rod. Furthermore, our method was accurate to 0.07 N and 7.5 mm in estimating point force magnitude and

location respectively. Finally, we demonstrated the feasibility of the method in actuated systems by applying the method to a tendon-driven continuum robot.

Future work could study real-time application to more complex continuum robots using an FBG array, which can output thousands of accurate strain measurements along the robot's backbone. Specifying a more appropriate prior distributed load function or the inclusion of additional data sources (e.g. base load or tip position) may significantly improve estimation accuracy.

As this approach continues to be adapted and refined, it could have many impacts across the spectrum of continuum and soft robotics. In minimally invasive surgery, accurate estimation of interaction forces will provide important safeguards against tissue damage and could enhance surgical performance through haptic feedback. For larger scale soft robots, the approach could enable advancements in whole arm manipulation, locomotion, and safe human-robot interaction.

APPENDIX A
WHITE NOISE NOTATION

Many of the differential equations in this paper (e.g. the main state equation (3)) imply that a derivative equals some function of white noise. Technically, these derivatives will not exist in general (e.g. simple Brownian motion (2) is not differentiable). In spite of this technicality, the "white noise notation" that we use is often used in robotics [47], [49] as well as stochastic modelling texts [64] to intuitively describe a system model. However, white noise notation should actually be interpreted as a representation of the more proper differential notation. For example, in linear systems driven by white noise, the white noise notation

$$\dot{\boldsymbol{x}}(t) = F(t)\boldsymbol{x}(t) + G(t)\boldsymbol{w}(t) \tag{20}$$

should be interpreted as the stochastic differential equation

$$\boldsymbol{dx}(t) = F(t)\boldsymbol{x}(t)dt + G(t)\boldsymbol{d\beta}(t) \tag{21}$$

where $\boldsymbol{\beta}(t)$ is the Brownian motion associated with white noise $\boldsymbol{w}(t)$ [64].

This differential notation highlights the stochastic integration necessary to obtain the solution process $\boldsymbol{x}(t)$. After carrying out the integration, deterministic functions for the mean and covariance statistics can be calculated:

$$\begin{aligned} \boldsymbol{m}_x &= \Phi(t,t_0)\boldsymbol{m}_x(t_0) \\ P_{xx} &= \Phi(t,t_0)P_{xx}(t_0)\Phi^T(t,t_0) \\ &\quad + \int_{t_0}^{t} \Phi(t,\tau)G(\tau)Q(\tau)G^T(\tau)\Phi^T(t,\tau)d\tau. \end{aligned} \tag{22}$$

The Gaussian process regression framework that we follow [49] does not require us to carry out stochastic integration computations. Instead it uses linearized-Gaussian estimation to compute the posterior mean and covariance functions directly with standard Riemannian integration. In other words, we skip from (20) directly to the deterministic functions of interest (22). Therefore, throughout this paper, we have opted to use the more accessible white noise notation.

REFERENCES

[1] D. C. Rucker, B. A. Jones, and R. J. Webster III, "A geometrically exact model for externally loaded concentric-tube continuum robots," *IEEE transactions on robotics*, vol. 26, no. 5, pp. 769–780, 2010.

[2] D. Trivedi, A. Lotfi, and C. D. Rahn, "Geometrically exact models for soft robotic manipulators," *IEEE Transactions on Robotics*, vol. 24, no. 4, pp. 773–780, 2008.

[3] J. Lock, G. Laing, M. Mahvash, and P. E. Dupont, "Quasistatic modeling of concentric tube robots with external loads," in *2010 IEEE/RSJ international conference on intelligent robots and systems*. IEEE, 2010, pp. 2325–2332.

[4] D. C. Rucker and R. J. Webster III, "Statics and dynamics of continuum robots with general tendon routing and external loading," *IEEE Transactions on Robotics*, vol. 27, no. 6, pp. 1033–1044, 2011.

[5] D. B. Camarillo, C. F. Milne, C. R. Carlson, M. R. Zinn, and J. K. Salisbury, "Mechanics modeling of tendon-driven continuum manipulators," *IEEE transactions on robotics*, vol. 24, no. 6, pp. 1262–1273, 2008.

[6] N. Simaan, R. Taylor, and P. Flint, "A dexterous system for laryngeal surgery," in *IEEE International Conference on Robotics and Automation, 2004. Proceedings. ICRA'04. 2004*, vol. 1. IEEE, 2004, pp. 351–357.

[7] M. W. Hannan and I. D. Walker, "Real-time shape estimation for continuum robots using vision," *Robotica*, vol. 23, no. 5, pp. 645–651, 2005.

[8] D. B. Camarillo, K. E. Loewke, C. R. Carlson, and J. K. Salisbury, "Vision based 3-d shape sensing of flexible manipulators," in *2008 IEEE International Conference on Robotics and Automation*. IEEE, 2008, pp. 2940–2947.

[9] D. Trivedi and C. D. Rahn, "Model-based shape estimation for soft robotic manipulators: The planar case," *Journal of Mechanisms and Robotics*, vol. 6, no. 2, p. 021005, 2014.

[10] R. Takano, H. Mochiyama, and N. Takesue, "Real-time shape estimation of kirchhoff elastic rod based on force/torque sensor," in *2017 IEEE International Conference on Robotics and Automation (ICRA)*. IEEE, 2017, pp. 2508–2515.

[11] C. Shi, X. Luo, P. Qi, T. Li, S. Song, Z. Najdovski, T. Fukuda, and H. Ren, "Shape sensing techniques for continuum robots in minimally invasive surgery: A survey," *IEEE Transactions on Biomedical Engineering*, vol. 64, no. 8, pp. 1665–1678, 2016.

[12] Y. Chitalia, N. J. Deaton, S. Jeong, N. Rahman, and J. P. Desai, "Towards fbg-based shape sensing for micro-scale and meso-scale continuum robots with large deflection," *IEEE robotics and automation letters*, vol. 5, no. 2, pp. 1712–1719, 2020.

[13] S. C. Ryu and P. E. Dupont, "Fbg-based shape sensing tubes for continuum robots," in *2014 IEEE International Conference on Robotics and Automation (ICRA)*. IEEE, 2014, pp. 3531–3537.

[14] S. Sefati, R. J. Murphy, F. Alambeigi, M. Pozin, I. Iordachita, R. H. Taylor, and M. Armand, "Fbg-based control of a continuum manipulator interacting with obstacles," in *2018 IEEE/RSJ International Conference on Intelligent Robots and Systems (IROS)*. IEEE, 2018, pp. 6477–6483.

[15] R. J. Roesthuis and S. Misra, "Steering of multisegment continuum manipulators using rigid-link modeling and fbg-based shape sensing," *IEEE transactions on robotics*, vol. 32, no. 2, pp. 372–382, 2016.

[16] M. Abayazid, M. Kemp, and S. Misra, "3d flexible needle steering in soft-tissue phantoms using fiber bragg grating sensors," in *2013 IEEE International Conference on Robotics and Automation*. IEEE, 2013, pp. 5843–5849.

[17] R. J. Roesthuis, M. Kemp, J. J. van den Dobbelsteen, and S. Misra, "Three-dimensional needle shape reconstruction using an array of fiber bragg grating sensors," *IEEE/ASME transactions on mechatronics*, vol. 19, no. 4, pp. 1115–1126, 2013.

[18] Y.-L. Park, S. Elayaperumal, B. Daniel, S. C. Ryu, M. Shin, J. Savall, R. J. Black, B. Moslehi, and M. R. Cutkosky, "Real-time estimation of 3-d needle shape and deflection for mri-guided interventions," *IEEE/ASME Transactions On Mechatronics*, vol. 15, no. 6, pp. 906–915, 2010.

[19] K. Xu and N. Simaan, "An investigation of the intrinsic force sensing capabilities of continuum robots," *IEEE Transactions on Robotics*, vol. 24, no. 3, pp. 576–587, 2008.

[20] ——, "Intrinsic wrench estimation and its performance index for multisegment continuum robots," *IEEE Transactions on Robotics*, vol. 26, no. 3, pp. 555–561, 2010.

[21] C. B. Black, J. Till, and D. C. Rucker, "Parallel continuum robots: Modeling, analysis, and actuation-based force sensing," *IEEE Transactions on Robotics*, vol. 34, no. 1, pp. 29–47, 2017.

[22] D. C. Rucker and R. J. Webster, "Deflection-based force sensing for continuum robots: A probabilistic approach," in *2011 IEEE/RSJ*

International Conference on Intelligent Robots and Systems. IEEE, 2011, pp. 3764–3769.
[23] B. Gonenc and I. Iordachita, "Fbg-based transverse and axial force-sensing micro-forceps for retinal microsurgery," in *2016 IEEE SENSORS*. IEEE, 2016, pp. 1–3.
[24] S. Elayaperumal, J. H. Bae, D. Christensen, M. R. Cutkosky, B. L. Daniel, R. J. Black, J. M. Costa, F. Faridian, and B. Moslehi, "Mr-compatible biopsy needle with enhanced tip force sensing," in *2013 World Haptics Conference (Whc)*. IEEE, 2013, pp. 109–114.
[25] L. Xu, M. I. Miller, J. Ge, K. R. Nilsson, Z. T. H. Tse, and M. P. Fok, "Temperature-insensitive fiber-optic contact force sensor for steerable catheters," *IEEE Sensors Journal*, vol. 16, no. 12, pp. 4771–4775, 2016.
[26] Y. Noh, S. Sareh, J. Back, H. A. Würdemann, T. Ranzani, E. L. Secco, A. Faragasso, H. Liu, and K. Althoefer, "A three-axial body force sensor for flexible manipulators," in *2014 IEEE International Conference on Robotics and Automation (ICRA)*. IEEE, 2014, pp. 6388–6393.
[27] U. Seibold, B. Kubler, and G. Hirzinger, "Prototype of instrument for minimally invasive surgery with 6-axis force sensing capability," in *Proceedings of the 2005 IEEE International Conference on Robotics and Automation*. IEEE, 2005, pp. 496–501.
[28] P. Valdastri, K. Harada, A. Menciassi, L. Beccai, C. Stefanini, M. Fujie, and P. Dario, "Integration of a miniaturised triaxial force sensor in a minimally invasive surgical tool," *IEEE transactions on biomedical engineering*, vol. 53, no. 11, pp. 2397–2400, 2006.
[29] H. Yuan, P. W. Y. Chiu, and Z. Li, "Shape-reconstruction-based force sensing method for continuum surgical robots with large deformation," *IEEE Robotics and Automation Letters*, vol. 2, no. 4, pp. 1972–1979, 2017.
[30] M. Mahvash and P. E. Dupont, "Stiffness control of surgical continuum manipulators," *IEEE Transactions on Robotics*, vol. 27, no. 2, pp. 334–345, 2011.
[31] M. Khoshnam, A. C. Skanes, and R. V. Patel, "Modeling and estimation of tip contact force for steerable ablation catheters," *IEEE Transactions on Biomedical Engineering*, vol. 62, no. 5, pp. 1404–1415, 2015.
[32] J. Back, L. Lindenroth, R. Karim, K. Althoefer, K. Rhode, and H. Liu, "New kinematic multi-section model for catheter contact force estimation and steering," in *2016 IEEE/RSJ International Conference on Intelligent Robots and Systems (IROS)*. IEEE, 2016, pp. 2122–2127.
[33] S. Hasanzadeh and F. Janabi-Sharifi, "Model-based force estimation for intracardiac catheters," *IEEE/ASME Transactions on Mechatronics*, vol. 21, no. 1, pp. 154–162, 2015.
[34] R. Xu, A. Yurkewich, and R. V. Patel, "Curvature, torsion, and force sensing in continuum robots using helically wrapped fbg sensors," *IEEE Robotics and Automation Letters*, vol. 1, no. 2, pp. 1052–1059, 2016.
[35] F. Khan, R. J. Roesthuis, and S. Misra, "Force sensing in continuum manipulators using fiber bragg grating sensors," in *2017 IEEE/RSJ International Conference on Intelligent Robots and Systems (IROS)*. IEEE, 2017, pp. 2531–2536.
[36] A. Bajo and N. Simaan, "Kinematics-based detection and localization of contacts along multisegment continuum robots," *IEEE Transactions on Robotics*, vol. 28, no. 2, pp. 291–302, 2011.
[37] M. Razban, J. Dargahi, and B. Boulet, "A sensor-less catheter contact force estimation approach in endovascular intervention procedures," in *2018 IEEE/RSJ International Conference on Intelligent Robots and Systems (IROS)*. IEEE, 2018, pp. 2100–2106.
[38] Q. Qiao, G. Borghesan, J. De Schutter, and E. Vander Poorten, "Force from shape—estimating the location and magnitude of the external force on flexible instruments," *IEEE Transactions on Robotics*, vol. 37, no. 5, pp. 1826–1833, 2021.
[39] C. D. Santina, R. L. Truby, and D. Rus, "Data–driven disturbance observers for estimating external forces on soft robots," *IEEE Robotics and Automation Letters*, vol. 5, no. 4, pp. 5717–5724, 2020.
[40] Z. Zhang, J. Dequidt, and C. Duriez, "Vision-Based Sensing of External Forces Acting on Soft Robots Using Finite Element Method," *IEEE Robotics and Automation Letters*, vol. 3, no. 3, pp. 1529–1536, jul 2018.
[41] Z. Zhang, A. Petit, J. Dequidt, and C. Duriez, "Calibration and External Force Sensing for Soft Robots Using an RGB-D Camera," *IEEE Robotics and Automation Letters*, vol. 4, no. 3, pp. 2356–2363, jul 2019.
[42] V. A. Aloi and D. C. Rucker, "Estimating loads along elastic rods," in *2019 International Conference on Robotics and Automation (ICRA)*. IEEE, 2019, pp. 2867–2873.
[43] V. Aloi, K. T. Dang, E. J. Barth, and C. Rucker, "Estimating forces along continuum robots," *IEEE Robotics and Automation Letters*, vol. 7, no. 4, pp. 8877–8884, 2022.
[44] J. Burgner-Kahrs, D. C. Rucker, and H. Choset, "Continuum robots for medical applications: A survey," *IEEE Transactions on Robotics*, vol. 31, no. 6, pp. 1261–1280, 2015.
[45] M. Russo, S. M. H. Sadati, X. Dong, A. Mohammad, I. D. Walker, C. Bergeles, K. Xu, and D. A. Axinte, "Continuum robots: An overview," *Advanced Intelligent Systems*, vol. 5, no. 5, p. 2200367, 2023.
[46] A. W. Mahoney, T. L. Bruns, P. J. Swaney, and R. J. Webster, "On the inseparable nature of sensor selection, sensor placement, and state estimation for continuum robots or "where to put your sensors and how to use them"," in *2016 IEEE International Conference on Robotics and Automation (ICRA)*. IEEE, 2016, pp. 4472–4478.
[47] P. L. Anderson, A. W. Mahoney, and R. J. Webster, "Continuum reconfigurable parallel robots for surgery: Shape sensing and state estimation with uncertainty," *IEEE robotics and automation letters*, vol. 2, no. 3, pp. 1617–1624, 2017.
[48] S. Anderson, T. D. Barfoot, C. H. Tong, and S. Särkkä, "Batch nonlinear continuous-time trajectory estimation as exactly sparse gaussian process regression," *Autonomous Robots*, vol. 39, no. 3, pp. 221–238, 2015.
[49] T. D. Barfoot, *State estimation for robotics*. Cambridge University Press, 2017.
[50] P. Furgale, C. H. Tong, T. D. Barfoot, and G. Sibley, "Continuous-time batch trajectory estimation using temporal basis functions," *The International Journal of Robotics Research*, vol. 34, no. 14, pp. 1688–1710, 2015.
[51] S. Lilge, T. D. Barfoot, and J. Burgner-Kahrs, "Continuum robot state estimation using gaussian process regression on se (3)," *The International Journal of Robotics Research*, vol. 41, no. 13-14, pp. 1099–1120, 2022.
[52] T. D. Barfoot and P. T. Furgale, "Associating uncertainty with three-dimensional poses for use in estimation problems," *IEEE Transactions on Robotics*, vol. 30, no. 3, pp. 679–693, 2014.
[53] S. Anderson and T. D. Barfoot, "Full steam ahead: Exactly sparse gaussian process regression for batch continuous-time trajectory estimation on se (3)," in *2015 IEEE/RSJ International Conference on Intelligent Robots and Systems (IROS)*. IEEE, 2015, pp. 157–164.
[54] T. Y. Tang, D. J. Yoon, and T. D. Barfoot, "A white-noise-on-jerk motion prior for continuous-time trajectory estimation on se (3)," *IEEE Robotics and Automation Letters*, vol. 4, no. 2, pp. 594–601, 2019.
[55] K. Qin, "General matrix representations for b-splines," *The Visual Computer*, vol. 16, no. 3-4, pp. 177–186, 2000.
[56] S. Lovegrove, A. Patron-Perez, and G. Sibley, "Spline fusion: A continuous-time representation for visual-inertial fusion with application to rolling shutter cameras." in *BMVC*, vol. 2, no. 5, 2013, p. 8.
[57] C. E. Rasmussen, "Gaussian processes in machine learning," in *Summer school on machine learning*. Springer, 2003, pp. 63–71.
[58] Y. Wang and G. S. Chirikjian, "Error propagation on the euclidean group with applications to manipulator kinematics," *IEEE Transactions on Robotics*, vol. 22, no. 4, pp. 591–602, 2006.
[59] ——, "Nonparametric second-order theory of error propagation on motion groups," *The International journal of robotics research*, vol. 27, no. 11-12, pp. 1258–1273, 2008.
[60] W. Park, Y. Wang, and G. S. Chirikjian, "The path-of-probability algorithm for steering and feedback control of flexible needles," *The International journal of robotics research*, vol. 29, no. 7, pp. 813–830, 2010.
[61] R. M. Murray, *A mathematical introduction to robotic manipulation*. CRC press, 2017.
[62] P. C. Hughes, *Spacecraft attitude dynamics*. Courier Corporation, 2012.
[63] D. C. Rucker, *The mechanics of continuum robots: model-based sensing and control*. Vanderbilt University, 2011.
[64] P. S. Maybeck, *Stochastic models, estimation, and control*. Academic press, 1982.

James M. Ferguson received the B.S. degree in mechanical engineering from The University of Tennessee, Knoxville, TN, USA, in 2016, and the Ph.D. degree in mechanical engineering from Vanderbilt University, Nashville, TN, USA, in 2022. His research interests include surgical and continuum robotics, image-guided surgery, and robot estimation and control.

D. Caleb Rucker (Senior Member, IEEE) received the B.S. degree in engineering mechanics and mathematics from Lipscomb University, Nashville, TN, USA, in 2006, and the Ph.D. degree in mechanical engineering from Vanderbilt University, Nashville, in 2011. He is currently an Associate Professor of Mechanical Engineering at The University of Tennessee, Knoxville, TN, USA, where he directs the Robotics, Engineering, and Continuum Mechanics in Healthcare Laboratory (REACH Lab). He co-founded and serves as Chief Science Officer of EndoTheia, Inc., Nashville, TN, USA. Dr. Rucker was a recipient of the NSF CAREER Award in 2017, and he has served as an Associate Editor for IEEE Transactions on Robotics.

Robert J. Webster III received the B.S. degree in electrical engineering from Clemson University, Clemson, SC, USA, in 2002, and the M.S. and Ph.D. degrees in mechanical engineering from Johns Hopkins University, Baltimore, MD, USA, in 2004 and 2007, respectively. Since 2008 he has been a faculty member at Vanderbilt University, Nashville, TN, USA, where he is the Richard A. Schroeder Professor of Mechanical Engineering, with appointments in Electrical Engineering, Otolaryngology, Neurological Surgery, Urologic Surgery, and Medicine. He directs the Medical Engineering and Discovery Laboratory, an NIH U01 Entrepreneurship Hub, and co-founded Vanderbilt Institute for Surgery and Engineering, which brings together physicians and engineers to solve challenging clinical problems. He co-founded and serves as President of Virtuoso Surgical, Inc., and EndoTheia, Inc., Nashville, TN, USA. He has received the IEEE RAS Early Career Award, the NSF CAREER Award, the RSS Early Career Spotlight Award, the IEEE Volz Award, and the Vanderbilt Engineering Award for Excellence in Teaching. He chaired the SPIE Image-Guided Procedures, Robotic Interventions, and Modeling conference, is an Executive Committee Member of the International Journal of Robotics Research, and served as Associate Editor of the IEEE Transactions on Robotics. His research interests include surgical robotics, image-guided surgery, and continuum robotics.